Xiao et al. Journal of Nanobiotechnology 2022, 20:410
https://doi.org/10.1186/s12951-022-01617-0

Journal of Nanobiotechnology

RESEARCH

Open Access

Hemin-incorporating DNA nanozyme enabling catalytic oxygenation and GSH depletion for enhanced photodynamic therapy and synergistic tumor ferroptosis

Xiaoxiong Xiao[2,3,4], Min Chen[6], Yuchen Zhang[7], Liang Li[5], Ying Peng[5], Junyu Li[1*†] and Wenhu Zhou[3,5*†]

Abstract

Photodynamic therapy (PDT) has emerged as a promising tumor treatment method via light-triggered generation of reactive oxygen species (ROS) to kill tumor cells. However, the efficacy of PDT is usually restricted by several biological limitations, including hypoxia, excess glutathione (GSH) neutralization, as well as tumor resistance. To tackle these issues, herein we developed a new kind of DNA nanozyme to realize enhanced PDT and synergistic tumor ferroptosis. The DNA nanozyme was constructed via rolling circle amplification, which contained repeat AS1411 G quadruplex (G4) units to form multiple G4/hemin DNAzymes with catalase-mimic activity. Both hemin, an iron-containing porphyrin cofactor, and chlorine e6 (Ce6), a photosensitizer, were facilely inserted into G4 structure with high efficiency, achieving in-situ catalytic oxygenation and photodynamic ROS production. Compared to other self-oxygen-supplying tools, such DNA nanozyme is advantageous for high biological stability and compatibility. Moreover, the nanostructure could achieve tumor cells targeting internalization and intranuclear transport of Ce6 by virtue of specific nucleolin binding of AS1411. The nanozyme could catalyze the decomposition of intracellular H_2O_2 into oxygen for hypoxia relief as evidenced by the suppression of hypoxia-inducible factor-1α (HIF-1α), and moreover, GSH depletion and cell ferroptosis were also achieved for synergistic tumor therapy. Upon intravenous injection, the nanostructure could effectively accumulate into tumor, and impose multi-modal tumor therapy with excellent biocompatibility. Therefore, by integrating the capabilities of O_2 generation and GSH depletion, such DNA nanozyme is a promising nanoplatform for tumor PDT/ferroptosis combination therapy.

Keywords: Nanomedicine, DNAzyme, Aptamer, Targeting, Phototherapy, Tumor hypoxia, Catalysis

Introduction

The development of effective strategies to manage malignant tumors is a long-lasting medical and pharmaceutical task, given the serious threaten of this disease towards human health [1]. Currently, tumor management highly depends on surgical resection, chemotherapy, radiotherapy, or their combinations, while the prognosis of these methods is usually poor with severe side-effects, achieving only limited clinical benefits for most of the patients. To this end, various novel therapeutic modalities have extensively explored to improve the therapeutic index, and several of them have made real clinic impact. Among these promising therapeutic strategies, photodynamic therapy (PDT) has attracted particular attention owing to its advantages of excellent spatial–temporal

†Junyu Li and Wenhu Zhou contributed equally to this work

*Correspondence: ndzhlyy1062@ncu.edu.cn; zhouwenhuyaoji@163.com

[1] Department of Radiation Oncology, Jiangxi Cancer Hospital, Nanchang, Jiangxi, China
[3] Xiangya Lung Cancer Center, Xiangya Hospital, Central South University, Changsha, Hunan, China
Full list of author information is available at the end of the article

controllability, low toxicity, non-invasiveness, and so on [2, 3]. During PDT process, the photosensitizers (PSs) are activated by light to convert the substrate of molecular oxygen into cytotoxic reactive oxygen species (ROS, mainly singlet oxygen $^1O_2$), which causes oxidative damage towards the bio-molecules of DNA, proteins and lipid within the illuminated area [4]. The PDT-based ROS damage could eradicate tumor through various mechanisms, such as directly killing tumor cells via inducing apoptosis or necrosis, impairing the tumor vasculatures, as well as causing tumor cells immunogenic death to trigger an anti-tumor immune response [5]. Owing to these advantages, PDT has been successfully translated into clinic to treat several types of tumors [6].

However, the wide clinical applications of PDT are still limited, and its efficacy is far from satisfactory due to the complex microenvironment of solid tumors. One typical pathological feature of tumor is hypoxia [7], which completely mismatches the basic requirement of PDT. Under hypoxic condition, the photodynamic efficiency is low because of the lack of molecular oxygen substrate. Even with ROS generation, the hypoxic cells are reported to be ~ threefold more resistant to ROS damage than aerobic cells [8]. The tumor cells are also equipped with various anti-oxidant defense systems to protect them from oxidative damage, in which the commonest mechanism is to employ tumor cell abundant glutathione (GSH) to scavenge ROS [9]. Moreover, the PDT process could further aggravate the tumor hypoxia by oxygen consumption and vascular impairment, which in turn activates multiple cell survival pathways to resist PDT [10, 11]. To this end, extensive research efforts have been made to reinforce the efficacy of PDT by relieving tumor hypoxia [12, 13]. For example, several studies tried to exploit hemoglobin and perfluorocarbon nanoparticles as O_2 carriers for tumor targeting O_2 delivery [14, 15], while the efficiency of such transient O_2 delivery methods is not high. Alternatively, particular research attention has been paid on the design of self-oxygen-supplying systems by using tumor abundant hydrogen peroxide (H_2O_2) as substrate to generate O_2. Such catalytic oxygenation can be achieved by catalase and some catalase-mimic nanozymes [16–18], which possesses the advantages of high efficiency, tumor specificity, and constant oxygen generation. In addition, several metal-based nanozymes hold the additional benefit of GSH depletion to further enhance PDT [19, 20].

While the catalytic oxygenation shows great promise to address the key limitations of PDT, the field is still in its infancy, and there also encompasses significant problems. For instance, tedious preparation procedures are required to load and deliver catalase, and the rapid deactivation and degradation of the enzyme is still an intractable problem. Nanozymes, by contrast, are much more stable and cost-effective, and can achieved tumor targeting delivery by rational surface modifications [21, 22], while the potential toxicities such as metal poisoning strongly restrict their in vivo applications [23, 24]. Moreover, it should also consider the effective PS loading to realize co-delivery, thus making the systems even more complicated. Therefore, the development of simple yet robust self-oxygenation methods that can facilely incorporate PSs are still deemed necessary for enhanced PDT.

It has been long though that all enzymes are proteins. With the progress of nucleic acids biology, the scope of enzymes has been significantly broadened since the discovery of various nucleic acids-based enzymes, including ribozymes and DNAzymes [25–27]. Specifically, ribozymes are found in nature, while DNAzymes are artificially isolated through a combinatorial process called in vitro selection. Currently, kinds of DNAzymes that can catalyze different types of chemical reactions have been discovered [28]. Compared to protein enzymes, DNAzymes are compared favorably for in vivo applications owing to high chemical stability, reversible catalytic activity under harsh conditions (e.g., temperature, organic solvents, wide ranges of pHs), and ease of versatile modifications and labeling with low immunogenicity [26]. Moreover, such DNA-based biomaterials are highly biocompatible and programmable to assemble into DNA nanostructures with controlled size, shape and morphology based on the Watson–Crick base-pairing rules [29], which innovates a new field of DNAzyme-based catalytic therapy [30–34]. Specifically, the catalase-mimic DNAzyme has been reported, which is formed by incorporating hemin into G-rich DNA sequences, and the resulting G-quadruplex (G4)-hemin DNAzyme could effectively decompose H_2O_2 to generate O_2.[35] Importantly, G4 DNA could also load chlorine e6 (Ce6, a widely used PS) with high efficiency [36], thus providing an "all-in-one" platform for in-situ oxygenation and photodynamic conversion. Strikingly, such elegant self-oxygen-supply and PS delivery system has been rarely applied for enhanced tumor PDT. The only example was reported by Yang and co-workers, who developed metal coordination-based nanoscale polymers to delivery G4 DNA systems for enhanced PDT therapy [36]. While the nanostructure is simply prepared, the coordination-based assembly system is prone to dissociation by various biological matrixes such as inorganic phosphate, metal ions, and serum [37, 38], resulting in pre-mature disassembly of the nanoparticles with inefficient tumor delivery. Therefore, it is still highly desired to develop effective delivery system for G4/hemin DNAzyme with Ce6 co-loading to allow stable in vivo circulation and tumor targeting accumulation.

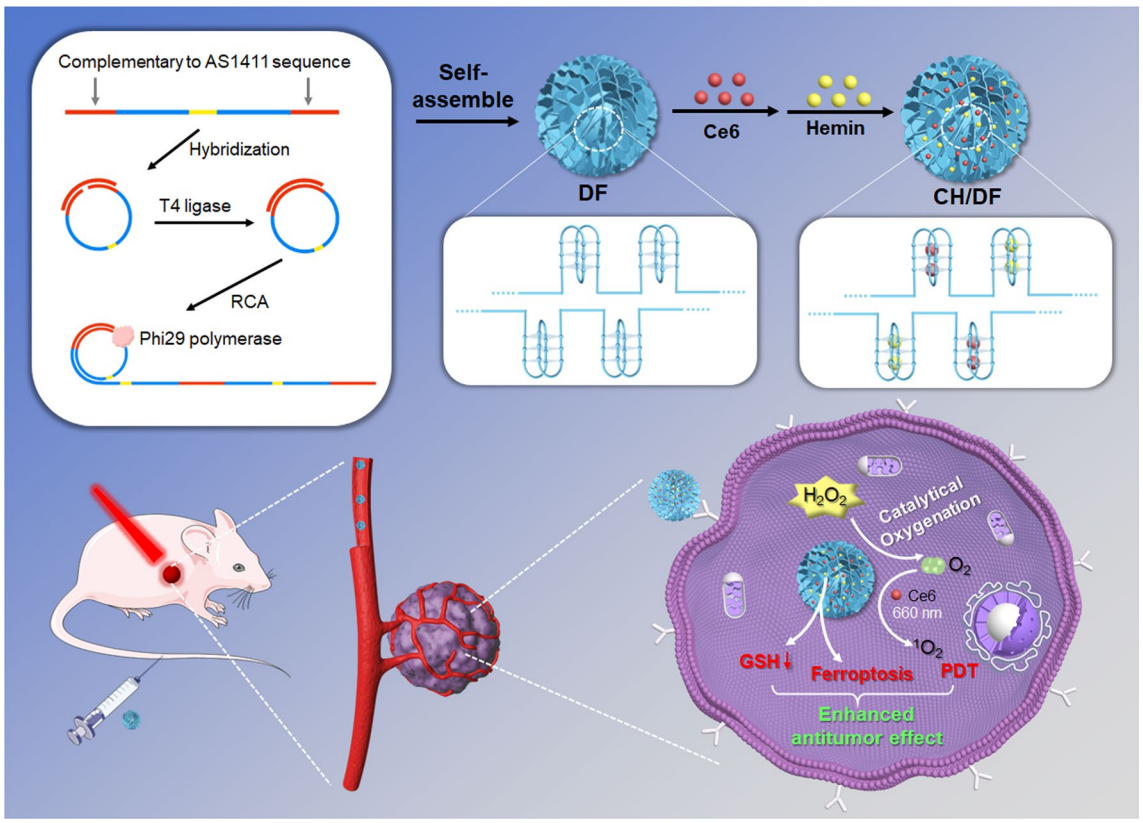

Scheme 1 Schematical showing the preparation of DF with AS1411 G4 motif for Ce6 loading and hemin incorporation for tumor targeting PDT/ferroptosis combinatorial therapy

Recently, we and other groups have demonstrated that DNA nanoflower (DF) is a type of highly robust nanocarrier to deliver functional nucleic acids [39, 40]. DF is a spherical porous DNA nanostructure formed by rolling circle amplification (RCA). Through rational design of DNA templates and primers, arbitrary DNA sequences can be facilely encoded into DF. By virtue of its high biocompatibility, programmability and predictability, such DNA nanostructure has been explored to deliver RNA-cleaving DNAzymes for gene silencing applications [41], while its attempt on G4/hemin DNAzyme system for tumor therapy has not been reported yet. Herein, we designed and fabricated a DF with incorporation of AS1411 sequence to realize enhanced PDT (Scheme 1). AS1411 is nucleolin-binding aptamer with G-rich sequence, which has been widely used as an active ligand for tumor targeting delivery [42, 43]. AS1411 could form a typical G4 structure in DF, which was not only a cargo for hemin and Ce6 loading, but also enabled active targeting delivery of the nanosystem into tumor cells. With hemin incorporation, the DF transformed into DNA nanozyme with catalase-mimic activity for in-situ oxygenation to relief tumor hypoxia. Therefore, the AS1411 unit in DF played multiple roles of a tumor targeting aptamer, a DNAzyme motif, as well as a drug loading domain. Compared with the free G4/hemin DNAzyme, the nanozyme displayed significantly improved biological stability, which was particularly important for in vivo applications. Moreover, hemin was found to have extra benefits to deplete intracellular GSH level and induce cell ferroptosis, both of which could further synergize with PDT for even better efficacy. Upon intravenous injection, the DNA nanozyme could effectively accumulate into tumor, and impose a robust PDT/ferroptosis combinatorial therapy to inhibit tumor growth with full biocompatibility.

Materials and methods

Materials, cells and animals

All DNA sequences (the primer: 5′-GTGGTGGTG TTGGTGGTGGT-3′. the template: Phosphate-CCA CCAACACCACCACCACCTTTGACACACTAGCGA TACGCGTATCGCTATGGCATATCGTACGATATG CCAGTGTGTCTTTCCACCA), deoxy-ribonucleoside triphosphate (dNTP) and bovine serum albumin (BSA) were purchased from Sangon Biotech Co., Ltd (Shanghai,

China). Phi29 DNA polymerase was from Lucigen Co., Ltd (USA). T4 ligase was obtained from Huamaike Bio Co., Ltd (Beijing, China). Hemin and Chlorin e6 (Ce6) were purchased from Frontier Scientific Co., Ltd (Utah, USA). Tris, KCl, NaCl, ammonium molybdate and H_2O_2 (30%) were from Sinopharm Co., Ltd (Shanghai, China). Singlet oxygen sensor green reagent (SOSG), 2′,7′-Dichlorofluorescin (DCFH-DA), GSH Assay Kit and Calcein-AM/PI were obtained from Solarbio Co., Ltd (Beijing, China). C11 BODIPY 581/591 was purchased from Glpbio Co., Ltd (CA, USA). Dulbecco's modified Eagle's medium (DMEM) and fetal bovine serum (FBS) were from Gibco Co., Ltd. Penicillin–streptomycin solution, 0.25% (w/v) trypsin solution, methyl thiazolyl tetrazolium (MTT) and 4′,6-diamidino-2-phenylindole (DAPI) were provided by Solarbio Co., Ltd (Beijing, China). Matrigel matrix was obtained from Biosciences Co., Ltd (New Jersey, US). Anti-Glutathione Peroxidase 4 (GPX4) Rabbit polyclonal was from Servicebio Co., Ltd (WuHan, China).

A549 cells and HEK-293 cells (human embryo kidney cells) were obtained from Xiangya cell center (Changsha, China). These cells were cultured in DMEM medium supplemented with FBS (10%), penicillin (1%, 50 U/mL) and streptomycin (1%, 50 U/mL) in a 5% CO_2 atmosphere (37 °C).

Female Balb/c mice (6 weeks old, ≈ 20 g) were purchased from Cavans Laboratory Animal Co., Ltd (Changzhou, China) and maintained in a sterile environment and allowed free access to food and water. All animal experiments were approved by the Experimental Animal Ethics Committee of Xiangya School of Pharmaceutical Sciences of Central South University and were carried out in accordance with the requirements the National Act on the Use of Experimental Animals (People's Republic of China).

Preparation of CH/DF

Synthesis of circular template: H_2O (69.5 μL), T4 ligase buffer (10×, 10 μL), template (10 μM, 6 μL) and primer (10 μM, 12 μL) were gently mixed and incubated at 95 °C for 10 min, then cooled to room temperature. T4 ligase was added and incubated at 25 °C for 4 h to close the circular DNA gap.

Preparation of DNA Flower (DF): Circular template (100 μL), dNTPs (10 mM, 40 μL), BSA (10×, 20 μL), phi29 polymerase (10 U/μL, 20 μL) and phi29 polymerase buffer (10×, 20 μL) were gently mixed in ice-bath, and incubated at 30 °C for 3 h and 75 °C for 10 min. The DNA flower was collected by centrifugation (20,000 rpm for 20 min) and washed twice with water, then mixed with buffer (20 mM Tris, 40 mM NaCl, 40 mM KCl, pH 7.6) in equal volume and incubated at room temperature for 1 h to form G4 structure.

Preparation of Ce6, hemin-loaded DNA Flower (CH/DF): DF was mixed with appropriate Ce6, incubated at room temperature for 4 h, Ce6-loaded DNA nanoflower (C/DF) was collected by centrifuged (20,000 rpm, 20 min) and washed twice with buffer. The preparation method of CH/DF was the same as that of C/DF. The above products were stored at − 20 °C.

Characterization of CH/DF

CH/DF was examined by the dynamic light scattering (DLS, Zetasizer Nano ZS90, Malvern Instruments, UK) to monitor the particle diameter, ζ-potential and polydispersity index. The morphological characteristics of CH/DF were evaluated using transmission electron microscopy (TEM, FEI, Oregon State, US) and scanning electron microscope (SEM, JSM-7900F, Tokyo, Japan). The encapsulation efficiency of drugs was calculated as follows: encapsulation efficiency = (weight of loaded drugs) / (weight of initially added drugs) × 100%. The encapsulation efficiencies of Ce6 and hemin were measured by Microplate Reader (Infinite M200, Tecan, Switzerland) and Visible–UV spectrophotometer (UV-2600, Shimadzu, Japan), respectively.

Catalytic activity test

The catalytic activity of CH/DF was determined by the Góth method. H_2O_2 (0.5 mL, 1 mM) and CH/DF (0.1 mL, 0.5 μM) were mixed and reacted at room temperature for 1 min. Then ammonium molybdate solution (0.5 mL, 32.4 mM) was added to form a yellow complex. After standing for 10 min, the catalase activity of CH/DF was determined by measuring the absorbance at 350 nm.

In vitro O_2 production and enhanced $^1O_2$ generation

To study the self-producing O_2 performance of CH/DF or CH/G4, the O_2 production was monitored the portable dissolved oxygen meter (JPBJ-609L, INESA Scientific Instrument Co., Ltd., China) every 10 s for 90 s. When O_2 level did not change, laser irradiation (660 nm, 0.75 W/cm^2) was added to study the dynamic change of O_2 of CH/DF. The $^1O_2$ production was tested by singlet oxygen sensor green (SOSG) probe after laser irradiation. Briefly, CH/DF (0.8 mL, 0.5 μM) was mixed with SOSG solution (0.1 mL, 25 μM). Then, H_2O_2 (0.1 mL, 100 mM) was added, and a continuous laser at 660 nm was applied with a power of 0.75 W/cm^2 every 10 s for 50 s. The fluorescence intensity of SOSG was measured by a fluorescence spectrophotometer (Ex = 490 nm, Em = 525 nm). To study the biological stability of the DNAzyme, the CH/DF or CH/G4 were pretreated with 10% FBS for 10 h, followed by the treatments as described above.

Cellular uptake study

A549 cells were seeded in 24-well plate at a density of 2×10^5 cells per dish overnight. Subsequently, CH/DF was added to incubated for 1 h, 2 h or 4 h. After washing three times with PBS, the cells were stained with DAPI, and the fluorescence was observed by fluorescence imaging system (Model No. CYTATION5, BioTek). Moreover, A549 cells and HEK-293 cells were utilized to investigate the specific uptake of CH/DF for tumor cells. To study the cell uptake mechanism of DF, a variety of inhibitors (chlorpromazine: the clathrin inhibitor; colchicine: the macropinocytosis inhibitor; nystatin: the caveolin inhibitor; NaN_3: ATP inhibitor) were used to intervene the endocytosis pathway. A549 cells were seeded with 2×10^5 cells per well in 24-well plate and incubated overnight. The cells were treated with chlorpromazine (10 μg/mL), colchicine (5 μg/mL), nystatin (15 μg/mL) or NaN_3 (1 mg/mL) for 30 min, and then CH/DF was added and incubated for 2 h. Fluorescence was observed and quantified by fluorescence imaging system (Model No. CYTATION5, BioTek).

In vitro cytotoxicity study

MTT assay was used to evaluate the cytotoxic effects of CH/DF to A549 cells. A549 cells were seeded with 5×10^3 cells per well in 96-well plate and incubated overnight, and then treated with a series of concentration dilutions of DF, C/DF and CH/DF (Ce6: 0.45, 0.9, 1.8, 3.6 and 7.2 μM; Hemin: 0.02, 0.04, 0.08, 0.16 and 0.32 μM) for 48 h. The C/DF and CH/DF groups were irradiated with laser (0.75 W/cm^2, 1 min) after incubation for 24 h. After that, the cells were washed twice with PBS and treated with the MTT reagent (5 mg/mL, 10 μL) for 4 h. Subsequently, the medium was removed and dimethyl sulfoxide (DMSO, 150 μL) was added. Finally, the UV–vis absorbance of each well was measured by Microplate Reader, and the cells viability was computed using the following formula:

Cell viability $= (A_{sample}/A_{control}) \times 100\%$, where A represents the absorbance at 570 nm.

To study the effect of ferroptosis inhibitors or inducers t, the cells were co-treated with CH/DF (Ce6: 1.6 μM) plus ferrostatin-1 (1 μM), glutathione (GSH, 1 mM), glutamic acid (1 mM), or erastin (10 μM), respectively. After culturing for 48 h, MTT assay was performed to measure the cell viability.

Live/Dead Staining assay

A549 cells were seeded with 2×10^5 cells per well in 12-well plate and treated with different formulations. The cells without any treatment were used as control. Subsequently, the cells were stained with both Calcein AM and PI, and observed by inverted fluorescent microscope (NIKON, Ti-S, Japan).

Intracellular ROS and LPO generation

DCFH-DA was used to evaluate the generation of intracellular ROS. A549 cells were seeded with 2×10^5 cells per well in 24-well plate and treated with different formulations (Ce6: 5 μM) for 6 h. The cells were washed with PBS three times and incubated with DCFH-DA (10 μM) for 30 min, and then irradiated for 1 min (0.75 W/cm^2). Finally, the fluorescence of DCFH-DA of cells was observed by fluorescence imaging system (Model No. CYTATION5, BioTek). C11 BODIPY 581/591 probe was used to detect LPO, and the detection method was similar to ROS.

Intracellular GSH level measurement

GSH assay kit was used to quantify the intracellular GSH level. A549 cells were seeded with 2×10^5 cells per well in 24-well plate and treated with different formulations (Hemin: 2 μM) for 24 h. Then, the C/DF and CH/DF groups were irradiated with laser and incubated for another 1 h. All cells were collected and lysed by liquid nitrogen, and the supernatants were collected by centrifugation (12,000 rpm, 10 min). Then, the supernatants were treated GSH assay kit and the absorbances were measured at 412 nm by Microplate Reader (Infinite M200, Tecan, Switzerland).

Western blot analysis of HIF-α protein expression

A549 cells were seeded with 4×10^6 cells per well in 6-well plate and treated with different formulations for 24 h. Cells were treated by RIPA buffer to collect total protein. Protein concentrations were determined by a BCA Protein Assay Kit (Dingguo changsheng, China). Then, proteins were run on polyacrylamide gel and were transferred to PVDF membranes. After blocking with 5% skim milk, the membranes were incubated with HIF-α polyclonal antibody and β-actin antibody overnight at 4 °C, and then incubated with horseradish peroxidase-conjugated secondary antibody for 1 h at room temperature. Finally, the proteins were visualized by the ChemiDoc MP Imaging System (Bio-Rad).

Construction of A549 xenograft tumor model

Six-week-old female BALB/c nude mice were used to establish the A549 xenograft tumor model. Briefly, A549 cells were collected and dispersed in PBS at a density of 2×10^7/mL, and then injected into the skin of mice subcutaneously (100 μL per mouse).

Biodistribution analysis

To study biodistribution, free Ce6 or CH/DF (Ce6: 2 mg/kg) was injected to A549 tumor-bearing mice intravenously. After 24 h administration, the mice were sacrificed and their primary organs (heart, liver, spleen, lung and kidney) and tumors were collected for ex vivo imaging with the IVIS Lumina XRMS Series III system (PerkinElmer, Waltham, MA).

In vivo antitumor efficacy and histological analysis

The A549 tumor-bearing mice with tumor volumes of approximately 100 mm^3 were randomly divided into 6 groups (n = 6 per group): (1) PBS group as the control; (2) DF; (3) C/DF; (4) C/DF + L; (5) CH/DF; (6) CH/DF + L (Ce6: 2.5 mg/kg, respectively). The preparations were injected through a tail vein, and tumors were irradiated with a laser irradiation (0.75 W/cm^2, 5 min) after 24 h of administration. Tumor sizes and body weights were recorded every other day after injection. Tumor volumes were calculated as follows: Volume = (length × width^2)/2.

On the 16th day, all mice were sacrificed, tumors were collected for the hematoxylin and eosin (H&E) staining, TdT-mediated dUTP nick-end labeling (TUNEL) staining, immunofluorescence (caspase-3 and GPX4) staining. All major organs were collected for H&E staining to evaluate the safety of formulations.

Statistical analysis

The data were expressed as mean ± SD on the basis of at least three independent experiments. One-way ANOVA analysis of variance was used to determine the statistical significance of the difference group. P value < 0.05 was considered statistically significant.

Results and discussions

Preparation and characterizations of CH/DF

The DF were prepared according to our previous report [39], in which the circular DNA template was first ligation by T4 ligase, followed by rolling circle amplifications (Fig. 1A). With rational sequence design of the template, the resulting DF contained a AS1411 aptamer region for functionalization [42, 43], and a double helix region for structure stabilization. The successful preparation of DF was dynamically monitored by hydrodynamic size, and TEM, gel electrophoresis (Additional file 1: Figure S1). The nanoparticles were rapidly formed in 3 h, while the size gradually increased from 100 to 350 nm based on TEM characterization. For effective tumor targeting

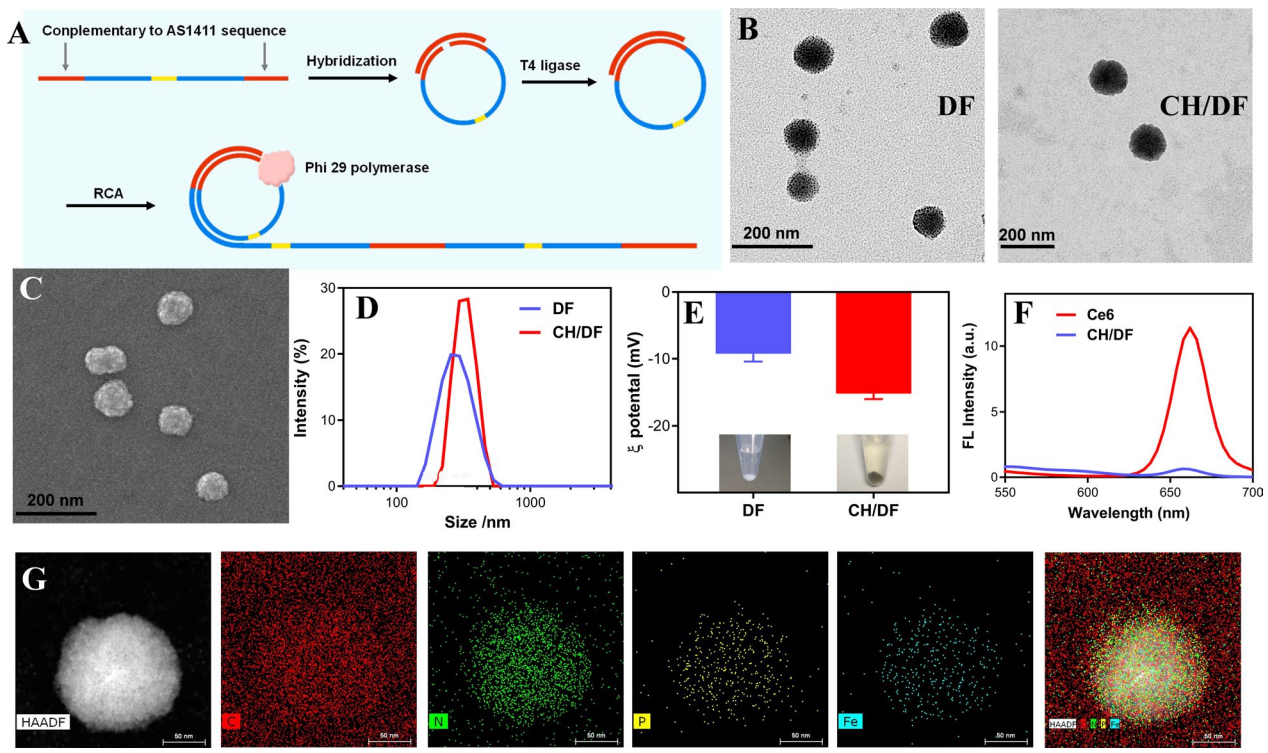

Fig. 1 **A** Schematic showing the design of template sequence and the preparation of DF. **B** The TEM micro-images of DF and CH/DF. **C** The SEM micro-image of CH/DF. **D** DLS and **E** surface charge measurements of DF and CH/DF. Inset: the appearance of the nanoparticles after centrifugation. **F** The fluorescence spectra of Ce6 before and after loading into DF. **G** The elemental mapping micro-image of CH/DF

delivery via EPR effect, the reaction time was chosen at 3 h with smaller particle size [44], and the structure of the resulting DF were presented in Fig. 1B and C, showing spherical morphology with uniformed size. Then, the photosensitizer of Ce6 and hemin were coloaded into DF via intercalation into AS1411 domain though π-π stacking, [36, 45] and the obtained CH/DF displayed slightly increased particle size (Fig. 1D), and even more negative surface charge (Fig. 1E). From TEM, the morphology and high dispersity of nanoparticles were maintained after Ce6 and hemin loading (Fig. 1B), while the appearance was changed from white color to purple (inset in Fig. 1E, the precipitants), suggesting the Ce6/hemin loading. Over a period of 24 h incubation, no obvious size change was observed in both PBS buffer and FBS-containing medium (Additional file 1: Figure S2), confirming its high colloidal stability for biological applications.

Upon loading into DF, the fluorescence intensity of Ce6 significantly weakened (Fig. 1F), attributable to the fluorescence quenching effect of G-quadruplex (G4) structure. Each DNA nanoflower was calculated to load 200 Ce6 molecules. In addition, the drug release profile of Ce6 was studied. Notably, Ce6 showed a typical pH-responsive release profile (Additional file 1: Figure S3), in which only 10% of the drug was released at pH 7.4 after 12 h, while the release significantly accelerated at pH 5.5. Such property is advantageous for prolonged in vivo circulation and rapid drug release after being delivered at target site. Meanwhile, the successful loading of hemin can be confirmed by the elemental mapping, in which the Fe and P signal was originated from hemin and the DNA payload, respectively (Fig. 1G).

In-situ oxygenation by DNA nanozymes for enhanced PDT

Upon intercalation of hemin into AS1411, a typical G4/hemin DNAzyme can be formed with peroxidase like activity [46]. Therefore, the CH/DF contained multiple DNAzyme units, which can be regarded as a type of DNA nanozymes. Such nanozyme could rapidly decompose H_2O_2 (Fig. 2A), accompanied by the generation of molecular oxygen (Fig. 2B). Without hemin loading, by contrast, the control DF did not show any catalytical activity, further confirming the formation of G_4/hemin DNAzyme. Free hemin also showed peroxidase characteristic, which is consistent with previous report [47]. While they share the same basic mechanism through oxidation–reduction of iron in hemin structure upon reaction with H_2O_2, the activity was strongly enhanced upon incorporation into G4 structure to form DNAzyme. We further tested the multiple turn-over of the reaction, and the nanoparticles could achieve similar O_2 generation rate after 3 cycles (Additional file 1: Figure S4), confirming its catalytic activity. The in-situ generated oxygen could in turn provide oxygen substrate for PDT. To demonstrate this, the PDT efficacy was monitored by measuring single oxygen ($^1O_2$) production using a SOSG probe. Upon laser irradiation, both C/DF (the DF with Ce6 alone loading) and CH/DF showed considerable efficacy for $^1O_2$ production (Additional file 1: Figure S5), indicating the photodynamic activity of Ce6 was retained after encapsulation into DF, although its fluorescence was quenched. Notably, further addition of H_2O_2 could significantly accelerate the efficacy of CH/DF but leaving C/DF being unaffected (Fig. 2C), which can be explained by DNAzyme-mediated catalytic generation of oxygen for enhanced PDT. Note that the tumor microenvironment was abundant with H_2O_2 owing to the Warburg effect of tumor cells [48]. Therefore, such enzyme system could act as an in-situ oxygen supplier at tumor site by employing tumor abundant H_2O_2 for effective PDT (Fig. 2D). To directly verify such oxygen-self-supply system, the H_2O_2 was added to allow O_2 generation, followed by a constant laser irradiation for 60 min (Fig. 2E). The O_2 level was still higher than the baseline in the end, demonstrating that the O_2 generation was sufficient for long-time PDT.

While DNA-based biomaterials are highly biocompatible, their in vivo applications are restricted due to non-specific interactions and degradation. For example, we previous found that serum proteins could bind with DNAzyme and affect its activity [49]. Upon integrating into DF, biological stability of the DNAzyme could be significantly enhanced, which can be attributed to the dense packaging of DNA in nanoflowers to prevent direct contact between nuclease and the inner layer of DNA molecules and retard the digestion process to a great extent [50, 51]. To verify this, we compared the catalytic activity of free G4/hemin DNAzyme and the DNAzyme-embedded DF. For parallel comparison with CH/DF, the same concentration of G4 DNA was used with equal loading amount of both Ce6 and hemin (termed CH/G4). As such, their catalytic activity and PDT effect were comparable in solution (Additional file 1: Figure S6). We then challenged them with serum to mimic in vivo circulation. After 12 h incubation, the catalytic activity of CH/DF was still maintained, while free CH/G4 DNAzyme displayed an obvious decrease of kinetics (Fig. 2F), indicating the deactivation of DNAzyme by biological matrixes. We previously showed that DNAzyme has high chemical stability in serum, but strong protein binding could passivate the enzymatic activity [49], which may explain the decrease of CH/G4 activity in serum. As a result, the oxygen generation was markedly reduced by twofold (Fig. 2G). Such different can be further reflected by $^1O_2$ generation upon laser irradiation, in which CH/DF exhibited much better PDT efficacy than CH/G4 after FBS pre-treatment (Fig. 2H). Therefore, DF could protect

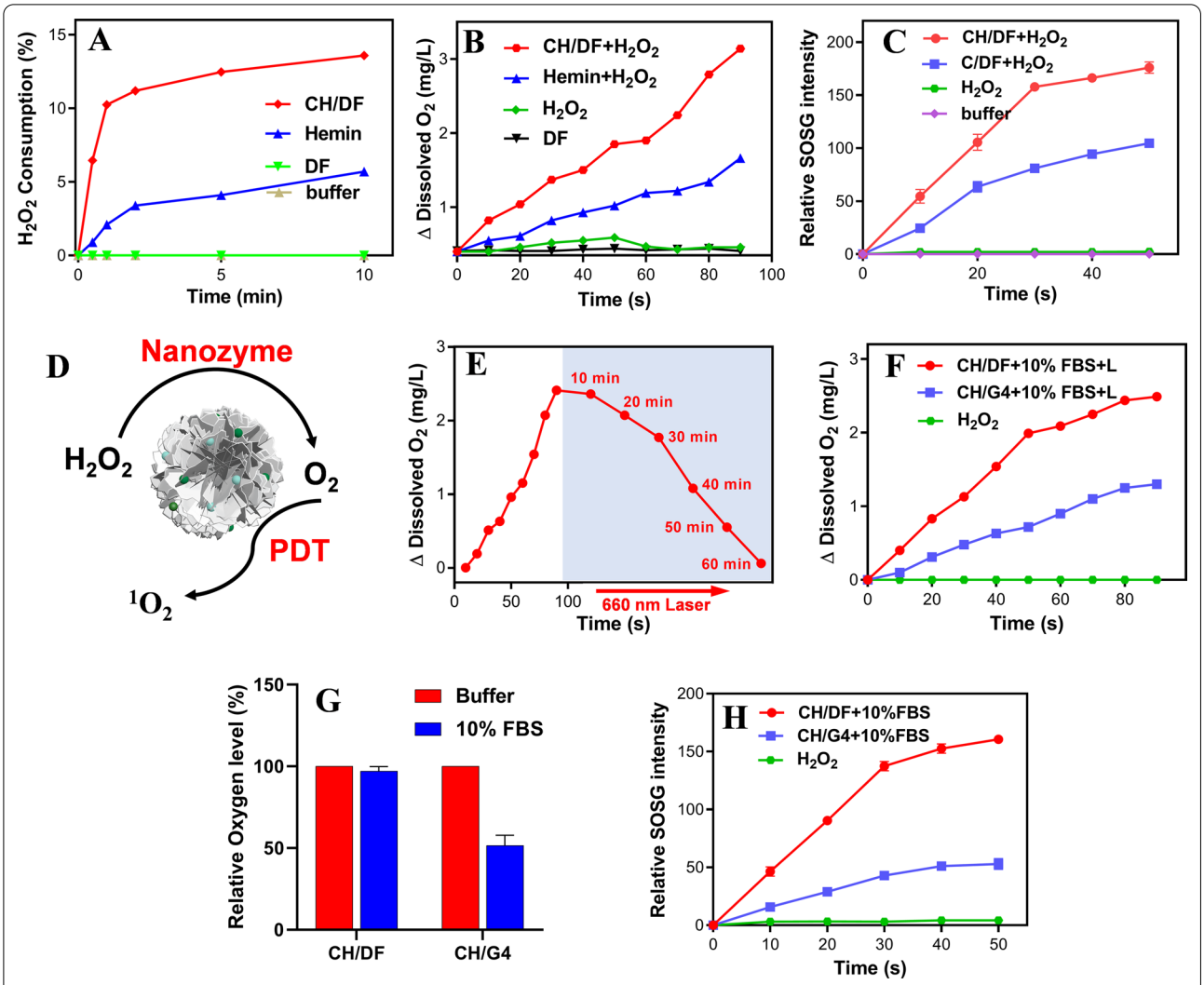

Fig. 2 **A** H_2O_2 consumption kinetics in presence of CH/DF, DF, and the buffer control. The kinetics of **B** O_2 and **C** $^1O_2$ generation for different reaction groups. **D** A carton showing the catalytic oxygenation for enhanced PDT. **E** The conceptual demonstration of self-oxygen-supply system. H_2O_2 was catalytically decomposed into molecular oxygen, and the laser was performed at 10 min for constant 60 min. **F** Catalytic oxygen generation for CH/DF and CH/G4 with 10% FBS pretreatment. **G** Relative amount of oxygen generation catalyzed by CH/DF and CH/G4 for 90 s with or without pretreatment of 10% FBS. **H** $^1O_2$ generation upon laser irradiation for CH/DF and CH/G4 with 10%FBS pretreatment

DNAzyme from deactivation under biological matrixes, and provides a robust nanocarriers to facilely integrate functional nucleic acids for in vivo applications.

Aptamer-mediated tumor cells targeting delivery

After systematical characterizations at test tube level, we then explored the intracellular performances of the nanoparticles. Each DF contained multiple AS1411 sequences in its structure, which was not only a domain for payloads loading, but also an active ligand for tumor targeting delivery by virtue of its high affinity with nucleolin that are overexpressed on tumor cells surface [52]. As a proof-of-concept demonstration, the nucleolin overexpressed A549 cancer cells were chosen. The intracellular transportation of the nanoparticles can be conveniently visualized owing to the intrinsic fluorescence of the loading Ce6. The fluorescence was gradually intensified overtime (Fig. 3A), and a bright signal was observed after 4 h incubation, indicating the effective nanoparticles internalization. We then tested the tumor targetability, and the HEK-293 normal cells were used as control. After 4 h incubation, obviously brighter fluorescence was observed in tumor cells than normal cells (Fig. 3B), resulting in ~ threefold higher intensity (Fig. 3C). Interestingly, we noticed a high co-localization of the nanoparticles with the cell nuclei, indicating the effective intranuclear

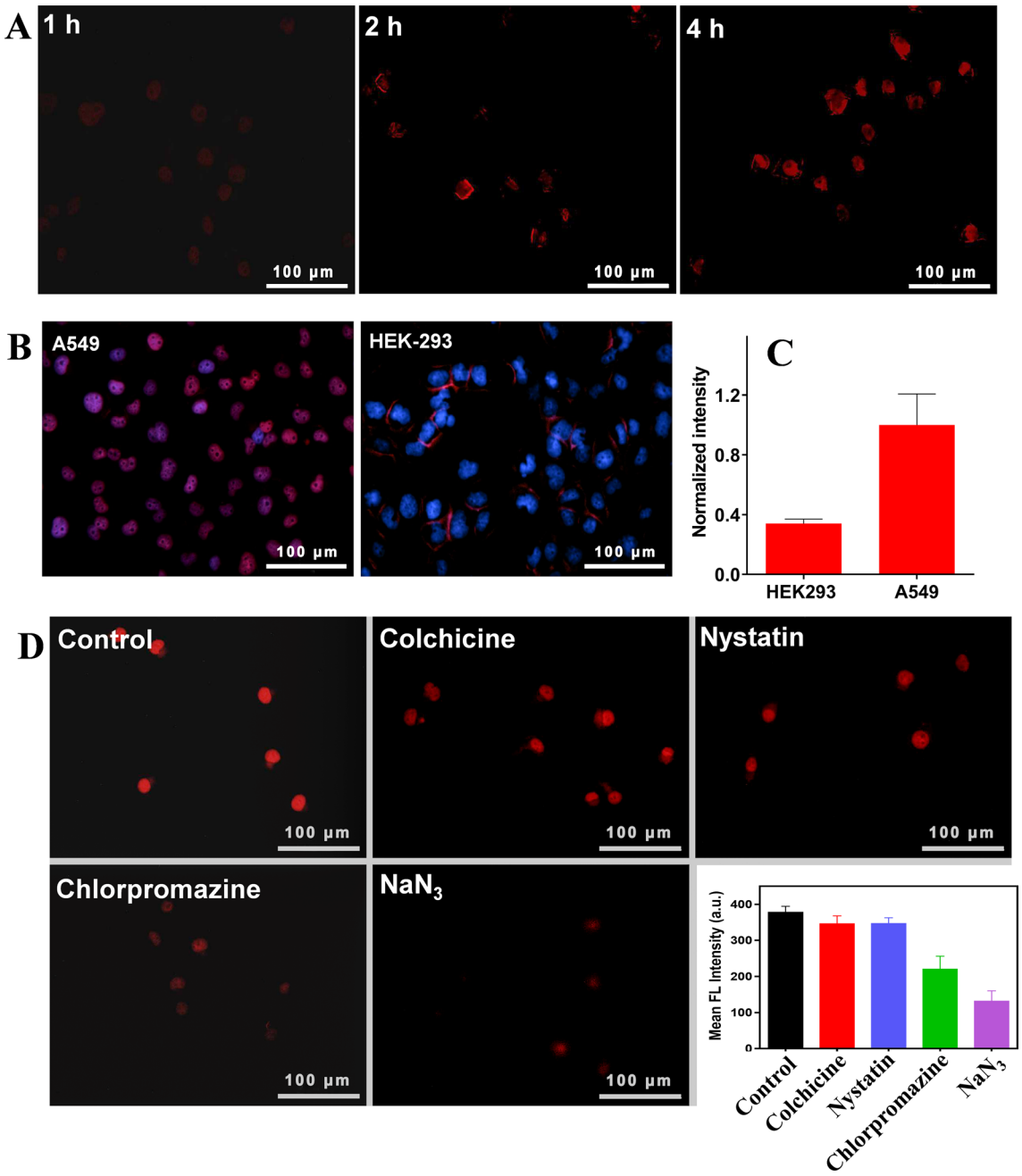

Fig. 3 **A** Fluorescence images showing the time-dependent internalization of the CH/DF into A549 cells. **B** Internalization of the nanoparticles by A549 and HEK-293 cells and **C** the intensity quantification. **D** Fluorescence images and intensity quantification indicating the effect of various probe ligands on cellular internalization of the nanoparticles

delivery. This can be attributable to high binding affinity of AS1411 for nucleolin to enable the subsequent intranuclear delivery. Since oxidative destruction of DNA is the important mechanism of PDT to kill tumor cells, such intranuclear delivery would enable the ROS generation within cell nuclei to directly destroy DNA for better PDT efficacy. To have a fundamental understanding, the delivery pathway was further explored by using various cell delivery pathway inhibitors (Fig. 3D) [53, 54]. Pre-treatment of colchicine and nystatin has little effect on internalization of the nanoparticles, indicating the minimal contribution of microtubular- and caveolae-mediated

endocytosis [54]. With chlorpromazine pretreatment, by contrast, the intracellular fluorescence was markedly weakened, consistent with previous report that DF was mainly delivered via clathrin-mediated endocytosis [41]. In addition, such pathway was energy-dependent as evidenced by the strong influence of NaN_3 pre-treatment.

Synergistic anti-tumor effect via PDT/ferroptosis combinatorial therapy

Having demonstrated the tumor targeting delivery, we then investigated the anti-tumor efficacy. Based on the MTT assay, DF was highly comparable with non-cytotoxicity on cells, while C/DF elicited marginal phototoxicity during treatment (Fig. 4A). CH/DF also showed noticeable cell suppression effect, which can be ascribed to the Fe-containing hemin to induce cell ferroptosis. Upon exposure to laser, the Ce6-loading DF showed concentration-dependent anti-tumor effect. Notably, CH/DF displayed much better efficacy than C/DF with significant decrease of IC_{50} value, suggesting the synergistic effect between each therapeutic modality. To confirm such result, Calcein-AM/PI co-staining was performed to visualize live and dead cells with green and red fluorescence, respectively (Fig. 4B). Bright green fluorescence was seen in DF group, in line with the high biocompatibility of such DNA-based carriers. For C/DF and CH/DF group, sparse red fluorescence was noticed, while the signal became strongly intensified after laser irradiation, in which all these observations were highly consistent with the above MTT assay.

Next, the anti-tumor mechanisms were studied in detail. Both PDT and ferroptosis could damage cells via generating large amount of ROS to damage cells, so the ROS level was first probed by using 2′,7′-dichlorofluorescin diacetate (DCFDA) with green fluorescence signal. The background ROS level was quite low, and DF or C/DF treatments barely showed any fluorescence (Fig. 4C). Notably, the green fluorescence turned on upon treatment with H/DF or CH/DF, owing to hemin-induced ferroptosis. The fluorescence was further enhanced in combination of PDT via laser irradiation, demonstrating their co-contribution for ROS generation.

To further identify the ferroptosis-based cell death pathway, intracellular lipid peroxidation (LPO) level, the specific indicator of ferroptosis, was probed by BODIPY-C11 (Fig. 4D). Obviously, all hemin-containing DF could produce green fluorescence inside cells, indicating LPO accumulation. Meanwhile, the LPO signal was further enhanced upon laser irradiation, confirming the sensitizing effect of PDT on ferroptosis. We also noticed that H/DF could produce much stronger fluorescence than free hemin, emphasizing the advantages of nanoparticles-mediated tumor cells targeting delivery. The contribution of ferroptosis-based anti-tumor effect was further examined by adding various ferroptosis inhibitors and promoters. Specifically, cytotoxicity of the nanoparticles was passivated upon addition of both ferroptosis inhibitor of ferrostatin-1 (Fer-1) and antidote of glutathione (GSH), but was enhanced by the promoters of glutamate (Glu) and erastin (Era) (Fig. 4E) [30]. All these results demonstrated the critical contribution of hemin-induced ferroptosis for tumor therapy.

For ROS-based anti-tumor mechanism, one key limitation is the GSH-mediated cell resistance [55]. Tumor cells has high GSH concentration (~10 mM), which could effectively scavenge a wide range of ROS to rescue ROS-induced cell damage. To this end, various GSH exhausting strategies have attempted to reinforce the efficacy of ferroptosis/PDT [56]. Fortunately, hemin has been reported to possess intrinsic activity to deplete GSH [57], which could benefit the therapeutic efficacy. To confirm such capability, we measured the intracellular GSH level. As expected, H/DF could effectively decrease the intracellular GSH level as compared to DF control (Fig. 4F). Interestingly, free hemin has little effect on GSH level, likely due to the fact that the negatively charged hemin is repelled by cell membrane with minimal internalization. Therefore, the incorporation of hemin into DF could facilitate its intracellular delivery.

In addition, the loading of hemin into AS1411 forms of peroxidase DNAzyme for in-situ oxygenation, which could solve the other restriction of PDT, i.e., tumor hypoxia. To demonstrate this concept, HIF-1α protein, the biomarker of the tumor hypoxia, was measured (Fig. 4G). Without any treatment, the tumor cells showed a considerable HIF-1α protein expression, and the hypoxia was further exacerbated with C/DF plus laser treatment, which can be attributable to the O_2 consumption during PDT. For CH/DF group, by contrast, the HIF-1α protein level was significantly reduced even under laser irradiation condition, confirming the capability of such self-oxygen-supply nanozyme to relief tumor hypoxia, which is highly important for tumor PDT in vivo.

(See figure on next page.)

Fig. 4 **A** The cytotoxicity of various treatments towards A549 tumor cells. **B** Calcein AM/PI double stain of A549 cells after various treatments. Scale bar, 200 μm. **C** Fluorescence images of the cells stained by DCFDA to probe ROS generation after various treatments. Scale bar, 100 μm. **D** Fluorescence images of the cells stained by BODIPY-C11 to probe LPO accumulation after various treatments. Scale bar, 100 μm. **E** The effect of various ferroptosis inhibitors/inducers on cytotoxic activity of CH/DF (with laser) towards tumor cells. **G** The expression of HIF-1α protein after various treatments

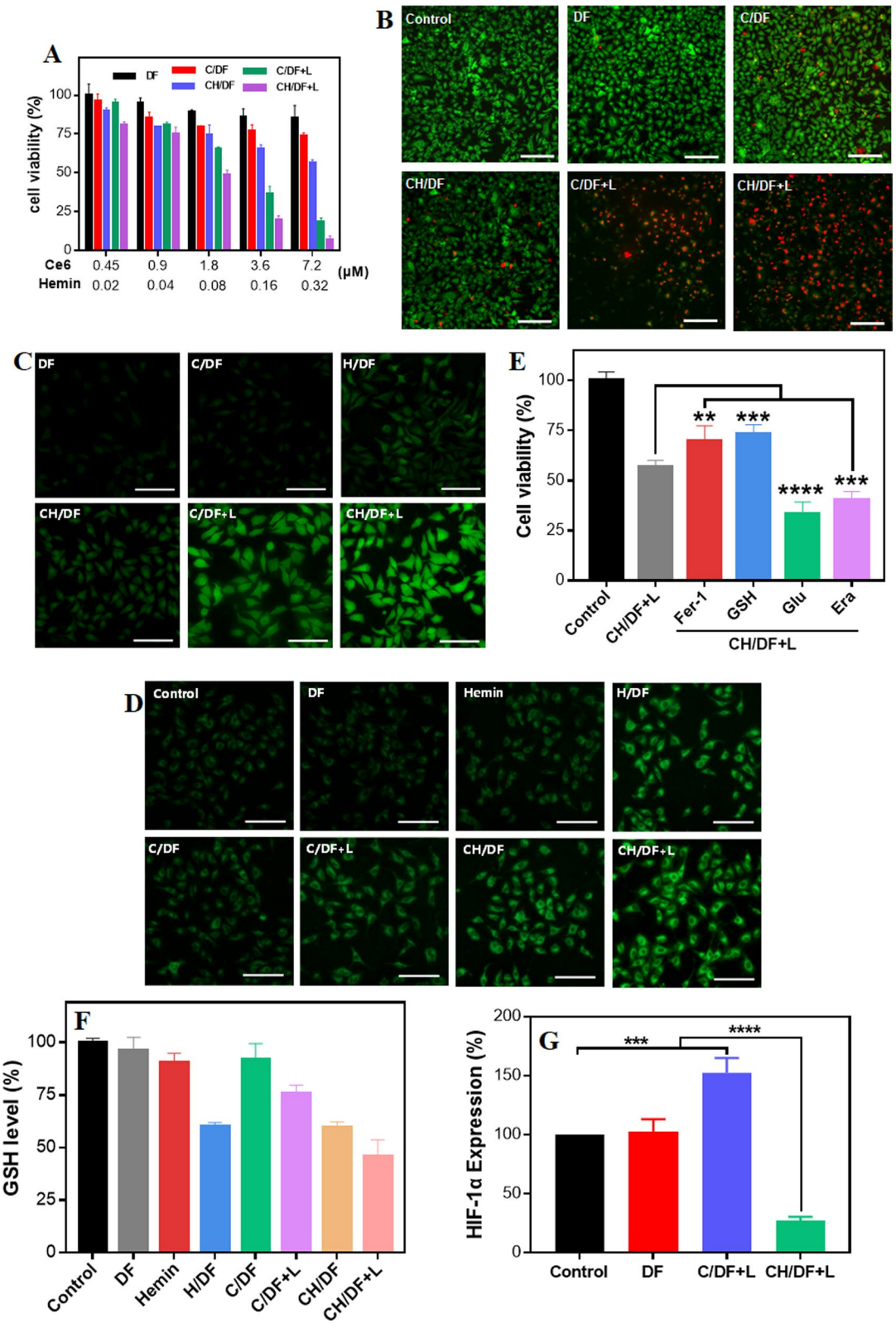

Fig. 4 (See legend on previous page.)

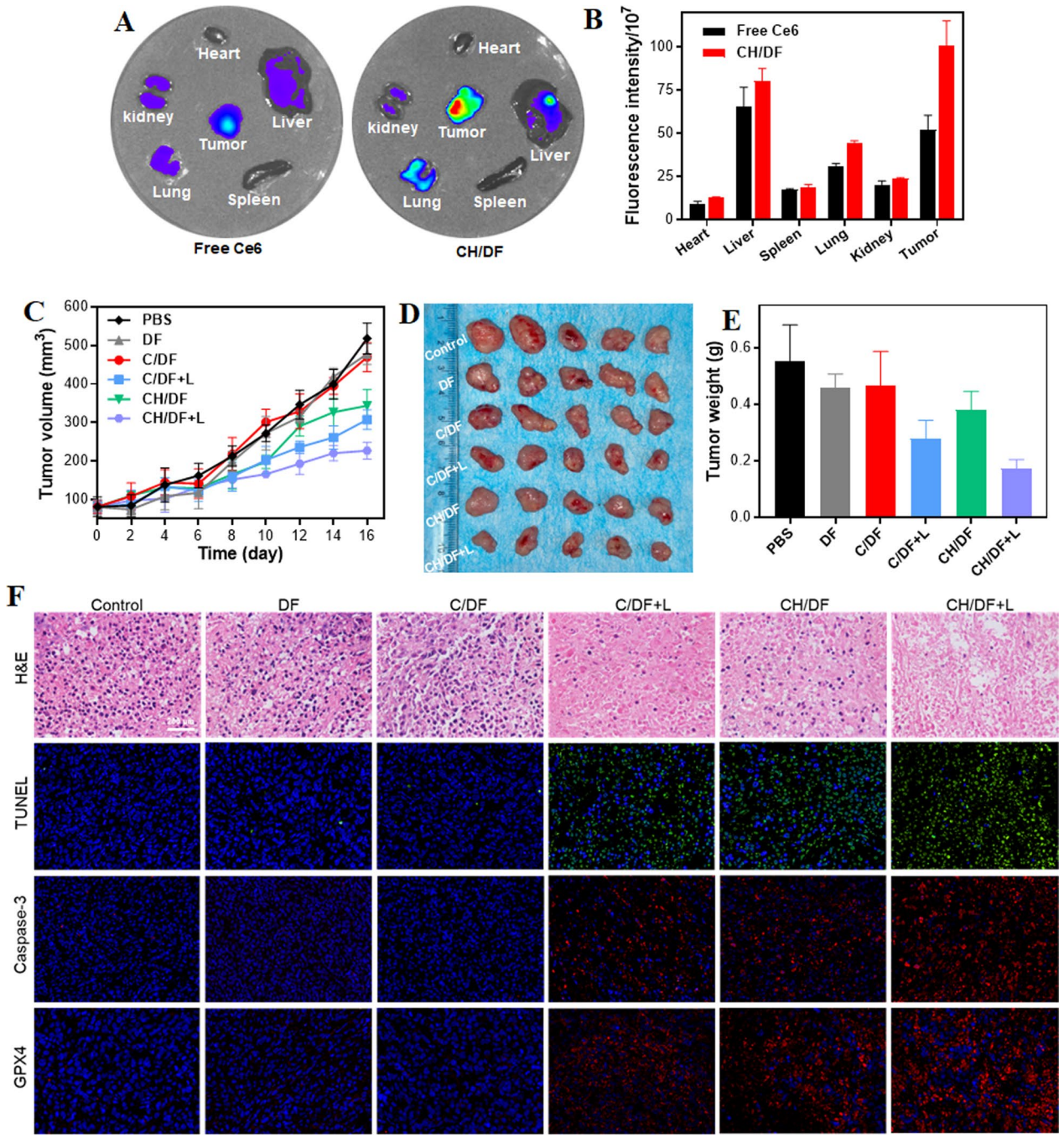

Fig. 5 **A** Ex vivo imaging the biodistribution of CH/DF and free Ce6 at 12 h post-injection into tumor bearing mice. **B** The intensity quantification at different organs based on the fluorescence images in **A**. **C** Dynamic monitoring the tumor growth after various treatments. **D** The appearance and **E** weight of the tumors at day 16 post various treatments. **F** Tumor H&E staining images, fluorescent staining of TUNEL and caspase-3 of the mice with different treatments

Targeting delivery of CH/DF for synergistic anti-tumor therapy in vivo

We next explored the in vivo performance of the nanosystem by using nude mice bearing subcutaneous A549 tumors. The biodistribution of CH/DF after intravenous injection was studied by fluorescence imaging to track the delivery of Ce6-containing nanoparticles. Due to the light penetration issue, the images were taken by collecting the main organs as well as tumor tissue for ex vivo observation (Fig. 5A). After 24 h circulation, the liver

showed the highest fluorescence intensity, since liver is the major organ to trap, metabolize, and eliminate nanoparticles [58]. Importantly, compared with free Ce6, CH/DF showed notably bright fluorescence at tumor site. We then quantified the intensity, and ~ twofold higher accumulation was observed for Ch/DF (Fig. 5B), demonstrating the tumor targeting delivery of the nanoparticles. Such targetability can be attributable to both EPR effect for passive accumulation and aptamer-mediated tumor cells selective recognition.

Motivated by the above results, we further applied the nanoparticles for tumor therapy. When the tumor volume reached ~ 100 mm^3, the mice were randomly divided into six groups, each receiving one of the following treatments with a single dose injection: PBS control, DF, C/DF, C/DF, C/DF plus laser, CH/DF, and CH/DF plus laser. Each formulation was administrated by intravenous injection, and only one dose was given. To monitor the efficacy, the tumor tissue was dynamically measured every other day, based on which the tumor growth curve was obtained (Fig. 5C). Without drugs loading, the DF merely showed any influence on tumor growth. C/DF without laser also failed to show any efficacy, while the tumor growth was suppressed upon laser irradiation, attributable to PDT effect. For CH/DF without laser, we also observed a notable tumor suppression activity, which was originated from hemin-mediated ferroptosis. With laser irradiation, the CH/DF showed an even stronger inhibition of tumor growth was seen, suggesting a combinatorial efficacy between ferroptosis and PDT. For direct observation, the mice were sacrificed and the tumor were collected for weighting (Fig. 5D, E), in which the results were highly consistent with the in vivo observation. Among various treatments, the CH/DF plus laser achieved the best therapeutic efficacy.

Then, the therapeutic efficacy was also evaluated by hematoxylin and eosin (H&E), TUNEL and caspase-3 staining of the tumors after treatments (Fig. 5F). Compared with the control, both DF and C/DF did not induce much pathological changes, confirming the high biocompatibility of the nanosystems. For the C/DF plus laser and CH/DF groups, by contrast, the tumors showed obvious necrotic responses, accompanied by the strong TUNEL and caspase-3 fluorescence, owing to the PDT and ferroptosis effect, respectively. Among them, CH/DF plus laser achieved the highest level of necrosis, apoptosis, and caspase-3 signal, verifying the combination effect of PDT/ferroptosis for enhanced anti-tumor therapy. Finally, the toxicity of each treatment was briefly studied. The body weight of all treating mice was unchanged during therapy (Additional file 1: Figure S7), and all major organs do not observe any obvious pathological abnormalities based on the H&E staining images (Additional file 1: Figure S8), indicating the high biocompatibility of the DF-based nanosystems with minimal side-effects.

Conclusions

In summary, we developed a DNA nanoreactor to simultaneously address several key limitations of PDT. The DNA nanostructure was facilely prepared via a well-defined protocol, and systematically characterized with uniformed size and morphology. All biological functions of such DNA nanostructure were derived from its multiple G4/hemin DNAzymes incorporation. First, as a type of catalase mimic DNAzyme, it allowed in situ self-oxygen-supply for enhanced PDT, and importantly, such nano-catalyst could resist biological degradation to enable in vivo applications. Second, the AS1411 G4 could also act as an active targeting ligand to mediate tumor cells selective internalization and intranuclear transportation for better therapeutic efficacy. Moreover, the loading hemin possessed extra functions to deplete intracellular GSH and induce cell ferroptosis, both of which synergized the anti-tumor effect of PDT. The nanostructure was further applied in tumor-bearing mice, which showed tumor targeting delivery and tumor growth inhibition via multiple anti-tumor mechanisms. Given its excellent biocompatibility and facile preparation, such DNA-based nanostructure holds great promise as multifunctional platform for tumor therapy.

Supplementary Information

The online version contains supplementary material available at https://doi.org/10.1186/s12951-022-01617-0.

Additional file 1. Characterization of DF formation by size, TEM and gel electrophoresis; colloidal stability of the nanoparticles; kinetics of drug release; catalytic multiple turn-over of the nanozymes; PDT effect; body weight change during treatments; H&E staining of the major organs.

Acknowledgements
Not applicable.

Author contributions
Conceived and designed the experiments: XX, JL and WZ. XX, and MC carried out the experiment. YZ and LL contributed to analyze the experimental results. YY: methodology, visualization. XX: methodology. JL and WZ wrote the manuscript. All authors read and approved the final manuscript.

Funding
This work was supported by Natural Science Foundation General Program of Hunan Province (2022JJ40830), Natural Science Foundation General Program of Changsha City (kq2014290), National Multidisciplinary Cooperative Diagnosis and Treatment Capacity Building Project for Major Diseases (Lung Cancer, grant number: z027002), Natural Science Foundation of Jiangxi (20192BAB205065) and the Excellent Young Scientists Fund of Jiangxi Cancer Hospital (2021EYS04).

Availability of data and materials
The raw data and processed data required to reproduce these findings are available from the corresponding author upon request.

Declarations

Ethics approval and consent to participate
All animal experiments were approved by the Experimental Animal Ethics Committee of Xiangya School of Pharmaceutical Sciences of Central South University (NO. 20220415T).

Consent for publication
Not applicable.

Competing interests
The authors declare that they have no competing interests.

Author details
[1]Department of Radiation Oncology, Jiangxi Cancer Hospital, Nanchang, Jiangxi, China. [2]Department of Thoracic Surgery, Xiangya Hospital, Central South University, Changsha, Hunan, China. [3]Xiangya Lung Cancer Center, Xiangya Hospital, Central South University, Changsha, Hunan, China. [4]National Clinical Research Center for Geriatric Disorders, Changsha, China. [5]Xiangya School of Pharmaceutical Sciences, Central South University, Changsha, Hunan, China. [6]Department of Thoracic Surgery, The Second People's Hospital of Huaihua City, Huaihua, China. [7]Department of Pharmacy, Yichun People's Hospital, Yichun, Jiangxi, China.

Received: 24 June 2022 Accepted: 31 August 2022
Published: 15 September 2022

References

1. Teo RD, Hwang JY, Termini J, Gross Z, Gray HB. Fighting cancer with corroles. Chem Rev. 2017;117:2711–29.
2. Liu P, Xie X, Shi XY, Peng Y, Ding JS, Zhou WH. Oxygen-self-supplying and HIF-1 alpha-inhibiting core-shell nanosystem for hypoxia-resistant photodynamic therapy. ACS Appl Mater Interfaces. 2019;11:48261–70.
3. Li X, Lee S, Yoon J. Supramolecular photosensitizers rejuvenate photodynamic therapy. Chem Soc Rev. 2018;47:1174–88.
4. Monro S, Colón KL, Yin H, Roque J, Konda P, Gujar S, et al. Transition metal complexes and photodynamic therapy from a tumor-centered approach: challenges, opportunities, and highlights from the development of TLD1433. Chem Rev. 2019;119:797–828.
5. Castano AP, Mroz P, Hamblin MR. Photodynamic therapy and anti-tumour immunity. Nat Rev Cancer. 2006;6:535–45.
6. Alsaab HO, Alghamdi MS, Alotaibi AS, Alzhrani R, Alwuthaynani F, Althobaiti YS, et al. Progress in clinical trials of photodynamic therapy for solid tumors and the role of nanomedicine. Cancers (Basel). 2020;12:20.
7. Gilkes DM, Semenza GL, Wirtz D. Hypoxia and the extracellular matrix: drivers of tumour metastasis. Nat Rev Cancer. 2014;14:430–9.
8. Fan YT, Zhou TJ, Cui PF, He YJ, Chang X, Xing L, et al. Modulation of intracellular oxygen pressure by dual-drug nanoparticles to enhance photodynamic therapy. Adv Funct Mater. 2019;29:78.
9. Meng X, Deng J, Liu F, Guo T, Liu M, Dai P, et al. Triggered all-active metal organic framework: ferroptosis machinery contributes to the apoptotic photodynamic antitumor therapy. Nano Lett. 2019;19:7866–76.
10. Huang L, Zhao SJ, Wu JS, Yu L, Singh N, Yang K, et al. Photodynamic therapy for hypoxic tumors: advances and perspectives. Coord Chem Rev. 2021;438:8.
11. Yang N, Xiao WY, Song XJ, Wang WJ, Dong XC. Recent advances in tumor microenvironment hydrogen peroxide-responsive materials for cancer photodynamic therapy. Nano-Micro Letters. 2020;12:8.
12. Jiang W, Delahunty IM, Xie J. Oxygenating the way for enhanced chemophototherapy. Theranostics. 2018;8:3870–1.
13. Wei FM, Rees TW, Liao XX, Ji LN, Chao H. Oxygen self-sufficient photodynamic therapy. Coord Chem Rev. 2021;432:8.
14. Shi XD, Yang WT, Ma Q, Lu Y, Xu Y, Bian KX, et al. Hemoglobin-mediated biomimetic synthesis of paramagnetic O-2-evolving theranostic nanoprobes for MR imaging-guided enhanced photodynamic therapy of tumor. Theranostics. 2020;10:11607–21.
15. Hu DR, Zhong L, Wang MY, Li HH, Qu Y, Liu QY, et al. Perfluorocarbon-loaded and redox-activatable photosensitizing agent with oxygen supply for enhancement of fluorescence/photoacoustic imaging guided tumor photodynamic therapy. Adv Funct Mater. 2019;29:12.
16. Liu P, Xie X, Shi X, Peng Y, Ding J, Zhou W. Oxygen-self-supplying and hif-1α-inhibiting core-shell nanosystem for hypoxia-resistant photodynamic therapy. ACS Appl Mater Interfaces. 2019;11:48261–70.
17. Wu H, Jiang Q, Luo KY, Zhu CP, Xie MM, Wang SG, et al. Synthesis of iridium-based nanocomposite with catalase activity for cancer phototherapy. J Nanobiotechnol. 2021;19:34.
18. Zhang Y, Wang FM, Liu CQ, Wang ZZ, Kang LH, Huang YY, et al. Nanozyme decorated metal-organic frameworks for enhanced photodynamic therapy. ACS Nano. 2018;12:651–61.
19. Zhu XL, Ni KY, Zhao ZH, Li MY, Huo LL, Zeng J, et al. Surface engineered iron oxide nanozyme for synergistic chemodynamic/ photodynamic therapy with glutathione depletion and hypoxia relief. Chem Eng J. 2022;440:99.
20. Feng LL, Liu B, Xie R, Wang DD, Qian C, Zhou WQ, et al. An Ultrasmall SnFe2O4 nanozyme with endogenous oxygen generation and glutathione depletion for synergistic cancer therapy. Adv Funct Mater. 2021;31:66.
21. Meng YC, Chen Y, Zhu JJ, Qi Y, Ding JS, Zhou WH. Polarity control of DNA adsorption enabling the surface functionalization of CuO nanozymes for targeted tumor therapy. Mater Horiz. 2021;8:972–86.
22. Sun WD, Xu YY, Yao Y, Yue J, Wu Z, Li HC, et al. Self-oxygenation mesoporous MnO2 nanoparticles with ultra-high drug loading capacity for targeted arteriosclerosis therapy. J Nanobiotechnol. 2022;20:9.
23. Liu P, Peng Y, Ding JS, Zhou WH. Fenton metal nanomedicines for imaging-guided combinatorial chemodynamic therapy against cancer. Asian J Pharm Sci. 2022;17:177–92.
24. Liu P, Shi XY, Zhong SH, Peng Y, Qi Y, Ding JS, et al. Metal-phenolic networks for cancer theranostics. Biomater Sci. 2021;9:2825–49.
25. Zhou WH, Liu JW. Multi-metal-dependent nucleic acid enzymes. Metallomics. 2018;10:30–48.
26. Zhou WH, Ding JS, Liu JW. Theranostic DNAzymes. Theranostics. 2017;7:1010–25.
27. Zhou WH, Saran R, Liu JW. Metal Sensing by DNA. Chem Rev. 2017;117:8272–325.
28. Huang PJJ, Liu J. In vitro Selection of Chemically Modified DNAzymes. Chemistry Open. 2020;9:1046–59.
29. Aliouat H, Peng Y, Waseem Z, Wang SF, Zhou WH. Pure DNA scaffolded drug delivery systems for cancer therapy. Biomaterials. 2022;285:9.
30. Liu P, Shi XY, Peng Y, Hu JM, Ding JS, Zhou WH. Anti-PD-L1 DNAzyme Loaded Photothermal Mn2+/Fe3+ Hybrid Metal-Phenolic Networks for Cyclically Amplified Tumor Ferroptosis-Immunotherapy. Adv Healthc Mater. 2022;11:677.
31. Xi Y, Xie X, Peng Y, Liu P, Ding JS, Zhou WH. DNAzyme-adsorbed polydopamine@MnO2 core-shell nanocomposites for enhanced photothermal therapy via the self-activated suppression of heat shock protein 70. Nanoscale. 2021;13:5125–35.
32. Liu P, Liu XJ, Cheng Y, Zhong SH, Shi XY, Wang SF, et al. Core-Shell Nanosystems for Self-Activated Drug-Gene Combinations against Triple-Negative Breast Cancer. ACS Appl Mater Interfaces. 2020;12:53654–64.
33. Nie YB, Li D, Peng Y, Wang SF, Hu S, Liu M, et al. Metal organic framework coated MnO2 nanosheets delivering doxorubicin and self -activated DNAzyme for chemo-gene combinatorial treatment of cancer. Int J Pharm. 2020;585:78.
34. Liu M, Peng Y, Nie YB, Liu P, Hu S, Ding JS, et al. Co-delivery of doxorubicin and DNAzyme using ZnO@polydopamine core-shell nanocomposites for chemo/gene/photothermal therapy. Acta Biomater. 2020;110:242–53.
35. Yang XJ, Fang CL, Mei HC, Chang TJ, Cao ZH, Shangguan DH. Characterization of G-Quadruplex/Hemin Peroxidase: Substrate Specificity and Inactivation Kinetics. Chem-Eur J. 2011;17:14475–84.
36. Yang Y, Zhu WJ, Feng LZ, Chao Y, Yi X, Dong ZL, et al. G-quadruplex-based nanoscale coordination polymers to modulate tumor hypoxia and achieve nuclear-targeted drug delivery for enhanced photodynamic therapy. Nano Lett. 2018;18:6867–75.

37. Guo LN, Chen Y, Wang T, Yuan Y, Yang YH, Luo XL, et al. Rational design of metal-organic frameworks to deliver methotrexate for targeted rheumatoid arthritis therapy. J Control Release. 2021;330:119–31.
38. Meng YC, Liu P, Zhou WH, Ding JS, Liu JW. Bioorthogonal DNA adsorption on polydopamine nanoparticles mediated by metal coordination for highly robust sensing in serum and living cells. ACS Nano. 2018;12:9070–80.
39. Ouyang Q, Liu K, Zhu QB, Deng HY, Le Y, Ouyang W, et al. Brain-Penetration and Neuron-Targeting DNA Nanoflowers Co-Delivering miR-124 and Rutin for Synergistic Therapy of Alzheimer's Disease. Small. 2022;18:210784.
40. Zhang KX, Liu JJ, Song QL, Wang DY, Shi JJ, Zhang HY, et al. Multifunctional DNA Nanoflowers for autophagy inhibition and enhanced antitumor chemotherapy. Chem J Chin Univ-Chin. 2020;41:1461–9.
41. Jin Y, Li ZH, Liu HF, Chen SZ, Wang F, Wang L, et al. Biodegradable, multifunctional DNAzyme nanoflowers for enhanced cancer therapy. Npg Asia Materials. 2017;9:365.
42. Zhou WH, Zhou YB, Wu JP, Liu ZB, Zhao HZ, Liu JW, et al. Aptamer-nanoparticle bioconjugates enhance intracellular delivery of vinorelbine to breast cancer cells. J Drug Target. 2014;22:57–66.
43. Wang SF, Zhao CT, Liu P, Wang Z, Ding JS, Zhou WH. Facile construction of dual-targeting delivery system by using lipid capped polymer nanoparticles for anti-glioma therapy. RSC Adv. 2018;8:444–53.
44. Ding YX, Xu YJ, Yang WZ, Niu P, Li X, Chen YD, et al. Investigating the EPR effect of nanomedicines in human renal tumors via ex vivo perfusion strategy. Nano Today. 2020;35:100970.
45. Poon LCH, Methot SP, Morabi-Pazooki W, Pio F, Bennet AJ, Sen D. Guanine-Rich RNAs and DNAs that bind heme robustly catalyze oxygen transfer reactions. J Am Chem Soc. 2011;133:1877–84.
46. Xu JQ, Jiang RD, He HL, Ma CB, Tang ZW. Recent advances on G-quadruplex for biosensing, bioimaging and cancer therapy. Trac-Trends In Analytical Chemistry. 2021;139:11657.
47. Qu R, Shen LL, Chai ZH, Jing C, Zhang YF, An YL, et al. Hemin-block copolymer micelle as an artificial peroxidase and its applications in chromogenic detection and biocatalysis. ACS Appl Mater Interfaces. 2014;6:19207–16.
48. Weber GF. Metabolism in cancer metastasis. Int J Cancer. 2016;138:2061–6.
49. Zhou WH, Chen QY, Huang PJJ, Ding JS, Liu JW. DNAzyme hybridization, cleavage, degradation, and sensing in undiluted human blood serum. Anal Chem. 2015;87:4001–7.
50. Zhang L, Zhu G, Mei L, Wu C, Qiu L, Cui C, et al. Self-assembled DNA immunonanoflowers as multivalent CpG nanoagents. ACS Appl Mater Interfaces. 2015;7:24069–74.
51. Zhu G, Hu R, Zhao Z, Chen Z, Zhang X, Tan W. Noncanonical self-assembly of multifunctional DNA nanoflowers for biomedical applications. J Am Chem Soc. 2013;135:16438–45.
52. Yazdian-Robati R, Bayat P, Oroojalian F, Zargari M, Ramezani M, Taghdisi SM, et al. Therapeutic applications of AS1411 aptamer, an update review. Int J Biol Macromol. 2020;155:1420–31.
53. Yang Y, Guo L, Wang Z, Liu P, Liu X, Ding J, et al. Targeted silver nanoparticles for rheumatoid arthritis therapy via macrophage apoptosis and Re-polarization. Biomaterials. 2021;264:120390.
54. Chen Y, Yang C, Mao J, Li H, Ding J, Zhou W. Spermine modified polymeric micelles with pH-sensitive drug release for targeted and enhanced antitumor therapy. RSC Adv. 2019;9:11026–37.
55. Liu P, Xie X, Liu M, Hu S, Ding JS, Zhou WH. A smart MnO2-doped graphene oxide nanosheet for enhanced chemo-photodynamic combinatorial therapy via simultaneous oxygenation and glutathione depletion. Acta Pharm Sin B. 2021;11:823–34.
56. Liu P, Zhou YB, Shi XY, Yuan Y, Peng Y, Hua SR, et al. A cyclic nano-reactor achieving enhanced photodynamic tumor therapy by reversing multiple resistances. J Nanobiotechnol. 2021;19:8.
57. Xuan W, Xia Y, Li T, Wang L, Liu Y, Tan W. Molecular self-assembly of bioorthogonal aptamer-prodrug conjugate micelles for hydrogen peroxide and ph-independent cancer chemodynamic therapy. J Am Chem Soc. 2020;142:937–44.
58. Ngo W, Ahmed S, Blackadar C, Bussin B, Ji Q, Mladjenovic SM, et al. Why nanoparticles prefer liver macrophage cell uptake in vivo. Adv Drug Del Rev. 2022;185: 114238.

Publisher's Note